Rational Design of Hierarchical MnO@N-doped Carbon Nanowires as a High-Performance Anode for Lithium-Ion Batteries

Xiaoming Xu[*], *Renzheng Li, Huanhuan Li, Donghai Hu, Jiaqi Fu*

School of Automotive and Traffic Engineering, Jiangsu University, Zhenjiang, China, 212013
[*]E-mail: xuxiaoming3777@163.com

A facile synthesis strategy for hierarchical MnO@N-doped carbon nanowires was developed using a single in situ pyrolysis of Mn-based coordination polymers. Core-shell MnO@N-doped carbon building blocks are interconnected into a mesoporous nanowire. The artificial nanocomposite facilitates fast transport of Li^+ ions and electrons and buffers the MnO volume change during Li insertion/extraction processes. As a consequence, hierarchical MnO@N-doped carbon nanowires display a promising electrochemical performance, such as a high reversible capacity, excellent cycling stability and rate capability, as an anode material for lithium-ion batteries.

1. INTRODUCTION

With the development of eco-friendly vehicles, novel lithium-ion batteries (LIBs) with excellent electrochemical properties, such as large capacity, long lifespan and high energy and power densities, are becoming more important. In recent years, 3d transition metal oxides (TMOs) (such as NiO [1,2], Co_3O_4 [3,4], Fe_3O_4 [5,6] and MnO [7,8]) have attracted attention as anode materials for LIBs because of their high theoretical capacities (>700 mAh g^{-1}) and novel conversion mechanisms [1-8]. Among them, MnO is attractive due to its high theoretical capacity (756 mAh g^{-1}), relatively low discharge voltage plateau, low cost and environmental benignity [7,8]. The MnO anode has disadvantages such as capacity fading, limited cycle lifespan and poor rate capability that prevent practical applications, and these problems originate from the low electrical conductivity and large volume change in MnO during repeated Li^+ uptake and release cycles [7,8]. Combining nanostructured MnO with a carbonaceous matrix is a feasible way to facilitate Li^+ ion and electron transport and

buffer the mechanical strain of lithiation/de-lithiation [8-10]. However, an innovative method to construct a MnO/carbon nanostructure with ideal lithium storage performance is needed.

Coordination polymers (CPs) assembled by multidentate organic ligands and metal ions have attracted attention because of their appealing structures and applications [11-13]. The abundance of organic ligands and secondary building units results in the diversity of the CP structures and morphologies [11-13]. Moreover, pyrolysis of CPs may simultaneously generate metals or metal oxides (from metal ion units) and a carbonaceous matrix (from organic ligands). Therefore, CPs are intriguing precursors or sacrificial templates for preparing TMO/carbon nanocomposites [14-16]. In this respect, searching for ideal CPs to rationally design TMO/carbon nanocomposites as high-performance anodes for LIBs is an ongoing research focus.

Here, we report a facile route to artificially fabricate hierarchical MnO@N-doped carbon nanowires with core-shell MnO@N-doped carbon building blocks through in situ carbonization of selected Mn-based CPs. The unique architecture of these structures motivated us to adopt them as anode materials for LIBs, and fascinating lithium storage properties, including a high reversible capacity, favourable cycling stability and excellent rate capability, were obtained.

2. EXPERIMENT

2.1 Mathematical model

All purchased chemicals were reagent grade and used without further purification. The Mn-NTA precursor was obtained according to the reported method [17]. In a typical procedure, 1.2 g of $MnCl_2 \cdot 4H_2O$ (J&K, 99%) and 0.6 g of nitrilotriacetic acid (NTA, Alfa Aesar, 98%) were added to a mixture of 30 mL of isopropyl alcohol (J&K, 99.5%) and 10 mL of distilled water with vigorous stirring. The mixture was then transferred into a 50 ml Teflon-lined autoclave, which was gradually heated to 180 °C and maintained for 12 h. After cooling, the white precipitates were filtered, washed with ethanol and distilled water, and then vacuum-dried at 100 °C for 6 h. To obtain hierarchical mesoporous MnO@N-doped carbon nanowires, the Mn-NTA precursor was calcined at 400 °C in N_2 for 2 h with a ramp of 2 °C min^{-1}.

2.2 Characterization

The phases of the obtained products were examined on a Bruker D8 Advance X-ray diffractometer (Cu Kα radiation, λ = 0.15406 Å). The morphologies of the samples were examined by field-emission scanning electron microscopy (SEM, FEI Nova NanoSEM450) equipped with an energy-dispersive X-ray spectroscopy (EDS) instrument and transmission electron microscope (TEM, JEOL, JEM-2100HR). Carbon and nitrogen contents in hierarchical MnO@N-doped carbon nanowires were obtained on a Perkin-Elmer 240C elemental analyser. Fourier transform infrared (FTIR) spectra were recorded in the range 400−4000 cm^{-1} on a Bruker TENOR 27 spectrophotometer using KBr pellets. PXRD measurements were recorded on a D/Max-2500 X-ray diffractometer using Cu Kα

radiation. Thermogravimetric analysis (TGA) was performed on a Labsys NETZSCH STA 449C Setaram apparatus with a heating rate of 5 °C min^{-1} in a nitrogen atmosphere. Nitrogen adsorption/desorption measurements (NOVA 2200e, Quantachrome Instruments) were performed to characterize the Brunauer-Emmett-Teller (BET) specific surface area and porous characteristics of the obtained MnO@N-doped carbon nanowires.

2.3 Electrochemical tests

The electrochemical performance of hierarchical MnO@N-doped carbon nanowires was investigated using coin-type cells (CR2032) assembled in an argon-filled glove box. The test electrodes were made from a mixture of the active material, BP2000 carbon black (BP, CABOT, S$_{BET}$ 1475 m^2 g^{-1}), and polyvinylidene fluoride (PVDF) binder with a weight ratio of 75:15:10. The electrolyte was 1 mol/L LiPF$_6$ in ethylene carbonate (EC)/diethyl carbonate (DEC) (1:1, v/v). Lithium foil was used as the counter electrode. Charge/discharge tests were performed between 0.01 and 3.0 V (vs. Li$^+$/Li) with a Land CT2001 C battery tester using various charge/discharge rates ranging from 100 mA g^{-1} to 1 A g^{-1} at room temperature.
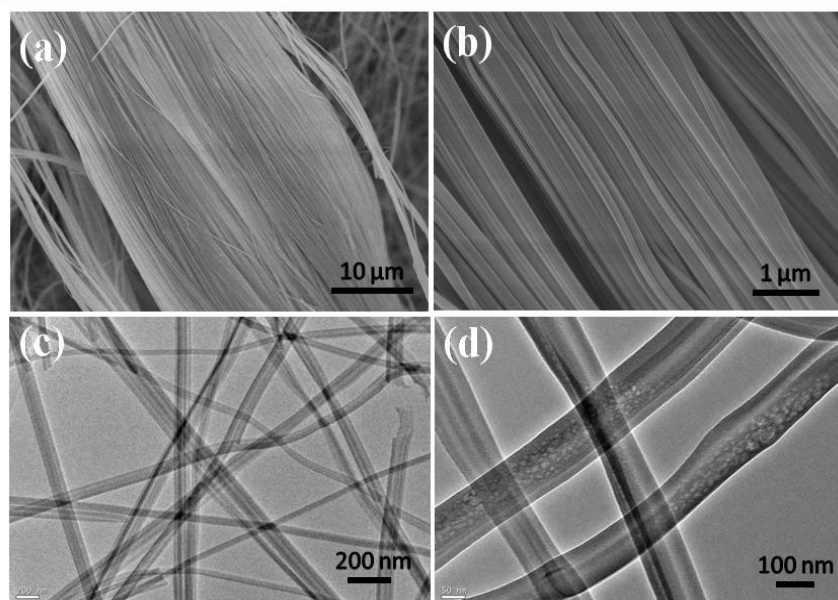
3. RESULTS AND DISCUSSION

Figure 1. SEM (a,b) and TEM (c,d) images of the Mn-NTA precursor.

Representative SEM images of the Mn-NTA precursor are shown in Fig. 1a and b. A large quantity of highly aligned, wire-like nanostructures with lengths of several to tens of micrometres can be observed in Fig. 1a. The nanowires have smooth surfaces and are bundled together (Fig. 1b). After

ultrasonication in ethanol, the bundles separated into single nanowires, as shown in the TEM images (Fig. 1c and d). The average diameter of the nanowires is approximately 150 nm.

The FTIR spectra of the NTA and Mn-NTA nanowires are shown in Fig. 2a. The peaks ranging from 3100 cm^{-1} to 2900 cm^{-1} are assigned to the stretching vibration of C–H [17]. Moreover, the peaks centred at 3041, 2989 and 2957 cm^{-1} in NTA shift to 2941, 2910 and 2850 cm^{-1} in Mn-NTA, respectively, indicating the introduction of Mn^{2+} coordination [17]. Additionally, characteristic peak located at 3426 cm^{-1} in Mn-NTA further confirms the coordination of Mn^{2+} [17]. Furthermore, the stretching vibration of C=O (1726 cm^{-1}) in NTA cannot be detected in Mn-NTA. However, a wide band composed of three peaks at 1674 cm^{-1}, 1649 cm^{-1} and 1582 cm^{-1} is observed, showing the formation of the –COOMn coordination group [18].

To investigate the thermal behaviour of the Mn-NTA coordinated nanowires in Ar, TGA and DTA curves were obtained and are shown in Fig. 2b. A 7.2% weight loss was observed before 100 °C, which is mainly due to the evaporation of absorbed water. Moreover, a noticeable weight loss occurred at approximately 350 °C due to the decomposition of Mn-NTA into MnO@C. Thus, calcination was performed at 400 °C for 2 h to ensure complete decomposition of the Mn-NTA precursor.
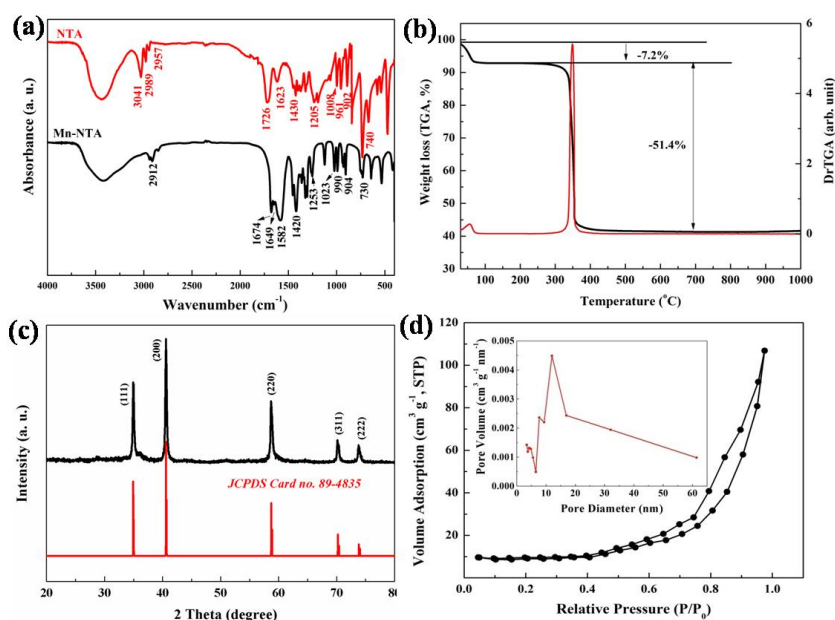

Figure 2. (a) FTIR spectra of the NTA and Mn-NTA nanowires. (b) TGA and DTA curves of the Mn-NTA nanowires. (c) XRD pattern of hierarchical MnO@N-doped carbon nanowires. (d) N_2 adsorption/desorption isotherm curves of hierarchical MnO@N-doped carbon nanowires. Inset shows the pore size distribution.

The XRD pattern of the obtained hierarchical MnO@N-doped carbon nanowires is shown in Fig. 2c. The crystalline phase of cubic MnO with the space group Fm-3m (JCPDS card no. 89-4853) can be observed. The crystalline carbon (graphite) peaks are barely visible due to the amorphous nature of the nanowires. The carbon and nitrogen contents are 13.7 and 3.9 wt%, respectively.

Therefore, the MnO@N-doped carbon nanocomposite was successfully produced via pyrolysis of the Mn-NTA precursor.

The nitrogen adsorption-desorption isotherms of hierarchical MnO@N-doped carbon nanowires are illustrated in Fig. 2d. A type-IV curve can be seen, indicating mesoporous characteristics. The specific surface area calculated according to the BET equation is 40.32 m^2 g^{-1}. Moreover, the maximum nitrogen adsorption is 108 cm^3 g^{-1}, resulting in a pore volume of 0.143 cm^3 g^{-1}. The dominant pore size from the Barrett-Joyner-Halenda (BJH) model is approximately 12 nm.
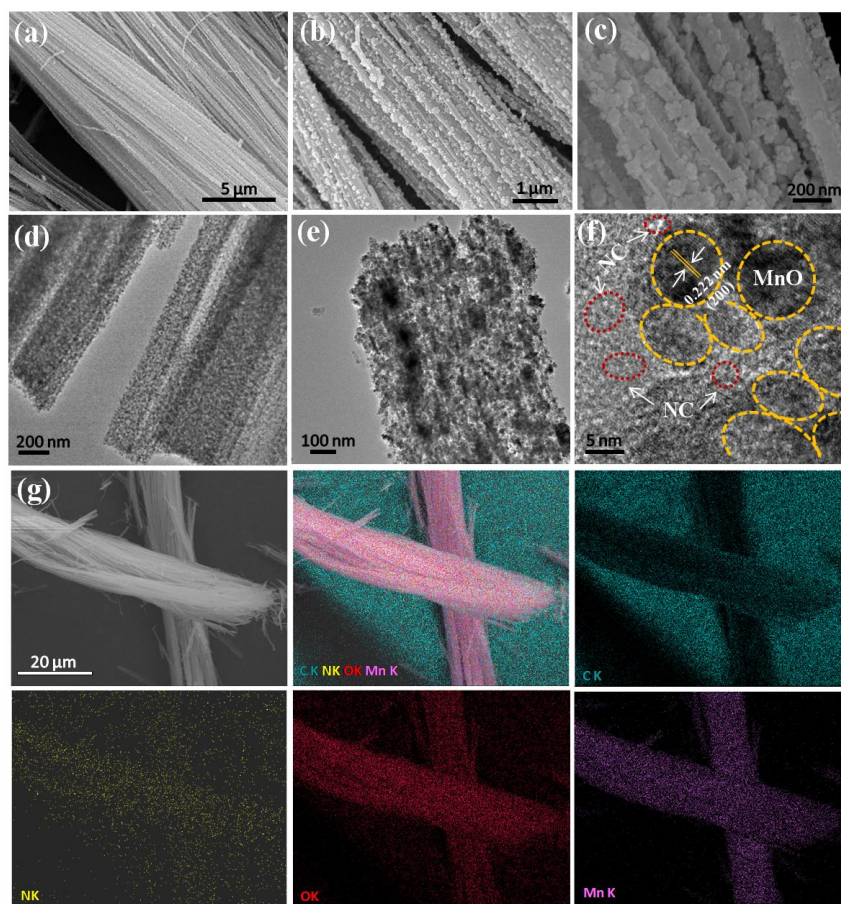

Figure 3. (a and b) SEM images of hierarchical MnO@N-doped carbon nanowires. (c) HRSEM image of hierarchical MnO@N-doped carbon nanowires. (d and e) TEM and (f) HRTEM images and atomic resolution lattice image of hierarchical MnO@C nanowires. (g) Elemental mapping images.

SEM images of the hierarchical MnO@N-doped carbon nanowires are shown in Fig. 3a-c. Individual nanowires can be observed in Fig. 3a, indicating that the morphology of the precursor is perfectly retained. The nanowires have porous and hierarchical structures and are assembled with many nanoparticles in the enlarged view (Fig. 3b and c). Further insight into the morphology of the prepared hierarchical MnO@N-doped carbon nanowires was obtained by TEM. The porous nanowires contain many connected nanosized subunits, as shown in Fig. 3d and e. The subunits seem to be

carbon-coated nanoparticles with an average diameter of 7 nm, as illustrated in the HRTEM image (Fig. 3f). No lattice fringes were detected for the carbon network, indicating its amorphous feature. Moreover, the interplanar spacing of 0.222 nm can be attributed to the (200) plane of MnO. The elemental distribution of hierarchical MnO@N-doped carbon nanowires is shown in Fig. 3g. The different colour regions indicate the uniform distributions of C, Mn, N and O throughout the sample.

Fig. 4a presents the initial three discharge/charge profiles of the hierarchical MnO@N-doped carbon nanowire electrode. The discharge/charge capacities of the first cycle are 1706.1/1101.3 mAh g^{-1}, leading to an initial Coulombic efficiency of 64.5%. The irreversible capacity loss might be a result of electrolyte decomposition and formation of an SEI film on the surface [8-10]. Moreover, the voltage plateau at 0.35 V in the first discharge curve is different from that of the other two discharge curves (0.40 V), indicating irreversible reactions during the first cycle. The charge/discharge curves of the second and third cycles almost overlap, showing the high reversibility of Li intercalation and de-intercalation.

Fig. 4b shows the first three CV curves of the hierarchical MnO@N-doped carbon nanowire electrode. The dominate peak in the first cathodic scan is located at 0.13 V and can be attributed to the reduction of Mn^{2+} to metallic Mn and regeneration of Li_2O [10, 19]. Two other peaks with low intensities are located at 1.85 V and 1.53 V, respectively, in the first cathodic scan and are due to the formation of an SEI film [20]. In the subsequent anodic scan, two oxidation peaks associated with the delithiation process are observed at 1.31 V and 2.08 V. Then, only one reduction peak is observed at 0.25 V, and two oxidation peaks are detected at 1.31 V and 2.08 V, indicating one-step lithiation and two-step delithiation [9, 10, 19]. Moreover, the curves are almost overlapped, suggesting the excellent reversibility of the lithiation/delithiation processes.

Fig. 4c shows the cycling performance of the hierarchical MnO@N-doped carbon nanowire electrode at a current density of 100 mA g^{-1}. The discharge/charge capacities continue decreasing during the first three cycles. Then, the capacities slowly increase during the subsequent fifty-four cycles, which may be due to the carbon activation process. Reversible discharge capacities of 1060, 1055, 1072, 1155, 1185 and 1170 mAh g^{-1} are achieved for the 4th, 10th, 20th, 50th, 75th and 100th cycles, respectively. Moreover, the Coulombic efficiency is higher than 98%, suggesting efficient lithiation/delithiation processes.

Fig. 4d shows the rate capability of the hierarchical MnO@N-doped carbon nanowire electrode at various current densities from 0.1 to 1 A g^{-1}. Discharge capacities of 1138, 1066, 900 and 770 mAh g^{-1} are observed at current densities of 0.1, 0.2, 0.5 and 0.8 A g^{-1}, respectively. A high discharge capacity of 700 mAh g^{-1} is obtained at a high current density of 1 A g^{-1}, which is much higher than the theoretical capacity of graphite (372 mAh g^{-1}). Interestingly, nearly the full capacity is recovered when the current density is reduced to 0.1 A g^{-1}.
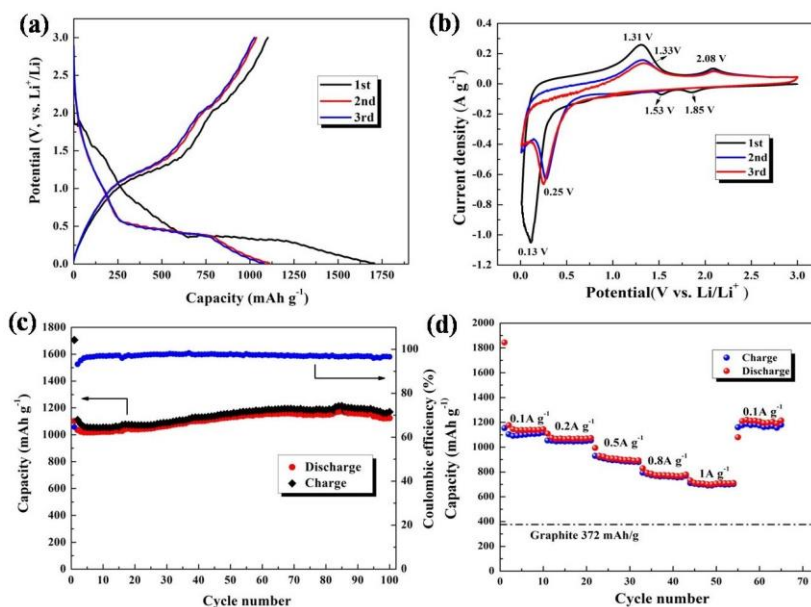
Figure 4. (a) The discharge/charge curves of the first three cycles for hierarchical MnO@N-doped carbon nanowires at a current rate of 100 mA g^{-1} between 0.01 and 3.00 V. (b) CV profiles of hierarchical MnO@N-doped carbon nanowires in the voltage range of 0.01 to 3.0 V (vs. Li$^+$/Li) and at a scan rate of 0.1 mV s^{-1}. (c) Cyclic performance of hierarchical MnO@N-doped carbon nanowires at 100 mA g^{-1}. (d) Cyclic performance of hierarchical MnO@N-doped carbon nanowires at different current densities.

Table 1. Comparison of the electrochemical performance of hierarchical MnO@N-doped carbon nanowires with that of reported MnO/C composite anodes.

Sample	Cycling performance	Rate capability
This work	1170 mAh g^{-1} at 0.1 A g^{-1} after 100 cycles	770 mAh g^{-1} at 0.8 A g^{-1}, 700 mAh g^{-1} at 1 A g^{-1}
Multi-porous MnO/N-doped carbon [21]	770.5 mAh g^{-1} at 0.3 A g^{-1} after 500 cycles	316.3 mAh g^{-1} at 1 A g^{-1}
Mesoporous Mn/C-N [22]	1085 mAh g^{-1} at 0.3 A g^{-1} after 100 cycles	877 mAh g^{-1} at 1 A g^{-1}, 552 mAh g^{-1} at 5 A g^{-1}
Tube-shaped MnO/C composite [23]	1057 mAh g^{-1} after 100 cycles	542 mAh g^{-1} at 1 A g^{-1}
Porous MnO/C [24]	861.3 mAh g^{-1} after 130 cycles	511.7 mAh g^{-1} at 0.8 A g^{-1}
Cross-linked MnO@C [25]	615 mAh g^{-1} after 100 cycles	497.4 mAh g^{-1} at 0.5 A g^{-1}
Biotemplated MnO/C microtubes [26]	610 mAh g^{-1} after 60 cycles	462 mAh g^{-1} at 1 A g^{-1}
MnO/C microsheets [27]	797.6 mAh g^{-1} after 50 cycles	429.4 mAh g^{-1} at 0.8 A g^{-1}
MnO/C composites [28]	740 mAh g^{-1} after 50 cycles	565 mAh g^{-1} at 1 A g^{-1}
MnO/C core-shell nanowires [29]	903 mAh g^{-1} after 60 cycles	610 mAh g^{-1} at 1 A g^{-1}
MnO multi-core@nitrogen-doped carbon shell nanoparticles [30]	578 mAh g^{-1} after 60 cycles	254 mAh g^{-1} at 1 A g^{-1}

According to the obtained experimental results, hierarchical MnO@N-doped carbon nanowires derived from an Mn-NTA precursor show an excellent electrochemical performance. Their attractive discharge capacities and rate capability are competitive with those of the previously reported MnO/C anode materials in Table 1 [17-23]. These properties might be due to the combination of the composition and structure of the hierarchical MnO@N-doped carbon nanowires, which buffer the volume change during Li$^+$ uptake/release, form a stable SEI film and facilitate ion and electron transport.

4. CONCLUSION

In conclusion, we report the construction of ultrasmall MnO nanoparticles embedded into hierarchical, porous N-doped carbon nanowires using Mn-NTA CPs as a self-sacrificial template. These distinctive hierarchical MnO@N-doped carbon nanowires exhibit a high reversible capacity, excellent cycling stability and rate capability as an anode material for LIBs. This present approach may be a versatile method for preparing transition metal oxide anode materials for LIBs.

CONFLICTS OF INTEREST
The authors declare no conflicts of interest.

References

1. C.Z. Wang, Y.J. Zhao, D.Z. Su, C.H. Ding, L. Wang, D. Yan, J.B. Li and H.B. Jin, *Electrochim. Acta,* 231 (2017) 272.
2. Y.Y. Feng, H.J. Zhang, Y. Zhang, Y.J. Bai and Y. Wang, *J. Mater. Chem. A,* 4 (2016) 3267.
3. S.W. Bian, L. Zhu, *RSC Adv.,* 3 (2013) 4212.
4. G.R. Wang, F.L. Zhu, J. Xia, L. Wang, Y.S. Meng and Y. Zhang, *Electrochim. Acta,* 257 (2017) 138.
5. Y. Huang, Z.H. Xu, J.Q. Mai, T.K. Lau, X.H. Lu, Y.J. Hsu, Y.S. Chen, A.C.H. Lee, Y.L. Hou and Y.S. Meng, *Nano Energy,* 41 (2017) 426.
6. C. Ding, Y.W. Zeng, L.L. Cao, L.F. Zhao and Q.Y. Meng, *ACS Appl. Mater. Interfaces,* 8 (2016) 7977.
7. Z.H. Cui, X.X. Guo and H. Li, *J. Power Sources,* 244 (2013) 731.
8. E. Samuel, H.S. Jo, B. Joshi, S. An, H.G. Park, Y.I. Kim, W.Y. Yoon and S.S. Yoon, *Electrochim. Acta,* 231 (2017) 582.
9. Y. Ding, L.H. Chen, P. Pan, J. Du, Z.B. Fu, C.Q. Qin and F. Wang, *Appl. Surf. Sci.,* 422 (2017) 1113.
10. B.L. Liu, D. Li, Z.J. Liu, L.L. Gu, W.H. Xie, Q. Li, P.Q. Guo, D.Q. Liu and D.Y. He, *Appl. Surf. Sci.,* 394 (2017) 1.

11. A. Raghuvanshi, C. Strohmann, J.B. Tissot, S. Clement, A. Mehdi, S. Richeter, L. Viau and M. Knorr, *Chem.-Eur. J.,* 23 (2017) 16479.
12. K. Das, A. Datta, S. Mendiratta, S.B. Mane, C. Massera, E. Garribba and C.H. Hung, *Inorg. Chim. Acta,* 469 (2018) 478.
13. X.F. Yang, H.B. Zhu and M. Liu, *Polyhedron,* 128 (2017) 18.
14. F.C. Zheng, Z.C. Yin, H.Y. Xia, G.L. Bai and Y.G. Zhang, *Chem. Eng. J.,* 327 (2017) 474.
15. Z.W. Zhao, T. Wen, K. Liang, Y.F. Jiang, X. Zhou, C.C. Shen and A.W. Xu, *ACS Appl. Mater. Interfaces,* 9 (2017) 3757.
16. H.H. Li, R.Y. Xu, Y.P. Wang, B.B. Qian, H.B. Wang, L. Chen, H.B. Jiang, Y.L. Yang and Y.Y. Xu, *RSC Adv.,* 4 (2014) 51960.
17. C.C. Li, L. Mei, L.B. Chen, Q.H. Li and T.H. Wang, *J. Mater. Chem.,* 22(2012) 4982.
18. G.X. Wang, X.L. Gou, J. Horvat and J. Park, *J. Phys. Chem. C,* 112(2008) 15220.
19. S.M. Guo, G.X. Lu, S. Qiu, J.R. Liu, X.Z. Wang, C.Z. He, H.G. Wei, X.R. Yan and Z.H. Guo, *Nano Energy,* 9(2014) 41.
20. C.C. Li, H. Yu, Q.Y. Yan and H.H. Hng, *Electrochim. Acta,* 187(2016) 406.
21. Q.X. Ye, J.J. Ru, J.H. Peng, G. Chen and D. Wang, *Chen. Eng. J.,* 331(2018) 570.
22. J.L. Niu, G.X. Hao, J. Lin, X.B. He, P. Sathishkumar, X.M. Lin and Y.P. Cai, *Inorg. Chem.,* 56(2017) 9966.
23. J.J. Ma, H.J. Wang, X.R. Liu, L.D. Lu, L.Y. Nie, X. Yang, Y.Q. Chai and R. Yuan, *Chem. Eng. J.,* 309(2017) 545.
24. Y.F. Xu, G.L. Xu, H. Su, Y. Chen, J.C. Fang, Q. Wang, L. Huang, J.T. Li and S.G. Sun, *J. Alloys Compd.,* 676(2016) 156.
25. X.Y. Zhou, T. Bai, J. Yang, K. Wen and C.W. Liu, *Ionics,* 22(2016) 779.
26. J.F. Wang, W. Liu, J.X. Chen, H.L. Wang, S. Liu and S.G. Chen, *Electrochim. Acta,* 188(2016) 210.
27. J.L. Liu, N. Chen and Q.M. Pan, *J. Power Sources,* 299 (2015) 265.
28. W.J. Zhu, H. Huang, W.K. Zhang, X.Y. Tao, Y.P. Gan, Y. Xia, H. Yang and X.Z. Guo, *Electrochim. Acta,* 152(2015) 286.
29. C.B. Zhang, J.G. Wang, D.D. Jin, K.Y. Xie and B.Q. Wei, *Electrochim. Acta,* 180(2015) 990.
30. H. Liu, Z.H. Li, Y.R. Liang, R.W. Fu and D.C. Wu, *Carbon,* 84(2015) 419.